

Joerg Reimann<sup>a</sup>, Jérôme Vicente<sup>b</sup>, Claudio Ferrero<sup>c</sup>†, Alexander Rack<sup>c</sup>, Yixiang Gan<sup>d</sup><sup>a</sup>Karlsruhe Institute of Technology, Karlsruhe, Germany<sup>b</sup>Polytech Marseille, Marseille, France<sup>c</sup>ERFSF-The European Synchrotron, Grenoble, France<sup>d</sup>The University of Sydney, Sydney, Australia

# 3d tomography analysis of the packing structure of spherical particles in slender prismatic containers

*Paper presented at the Symposium “Tomographic and Radiographic Imaging with Synchrotron X-rays and Neutrons” of the MSE 2018, 26–28 September 2018, Darmstadt, Germany*

In granular media, topological features are known to determine the effective material properties and boundary behavior when interacting with other structural components. X-ray computed tomography results are reported on sphere packing structures in slender prismatic containers ( $X = 20$ ,  $Y = Z = 80$  mm), filled and vibrated with both monosized spheres (diameter  $d = 2.4$  mm), Exp. (M), and polydisperse spheres ( $1 \text{ mm} < d < 1.25$  mm), Exp. (P). Packing structures were characterized by void fraction distributions, coordination numbers, contact angle distributions and Voronoi packing fractions. In (M), an almost perfect hexagonal dense packing exists in the total volume, associated with a packing fraction  $\gamma_t \approx 0.68$ . In additional packing experiments, large  $\gamma_t$  values were achieved as well. Although the  $d$  spread in (P) is relatively small, significantly different results are obtained:  $\gamma_t \approx 0.62$ , regular structures are restricted to narrow wall zones and distributions in the container volume are nonhomogeneous. It is argued that the small degree of ordered structure is a characteristic feature of polydispersity for efficiently vibrated sphere packings.

**Keywords:** Monosized spheres; Polydisperse spheres; Packing fraction; X-ray tomography; Prismatic container;

## 1. Introduction

Packings of spherical particles play an important role in many technical applications where mechanical or heat and mass transfer issues are of prime importance [1–4]. In solid state physics, monosized sphere systems are used for simulating crystallization processes in order to study the emergence of order [5, 6].

Historically, first investigations were limited to determine the main global structural property in containers, the packing fraction  $\gamma_t$ , defined as the ratio of the volume occu-

ried by the particles to the total packing volume (with the corresponding porosity or void fraction  $\varepsilon_t = 1 - \gamma_t$ ). Systems with one nominal sphere diameter  $d$  (mono-sized spheres) were investigated as well as mixtures of spheres with two or more diameters (binary, ternary systems) and systems with diameter distributions (polydisperse spheres), see e.g. McGeary [7]. It should be stated that in several of these experimental investigations the particle specifications were not precisely defined with respect to sphericity, roughness, diameter tolerances. Furthermore, the applied densification methods (tapping, vibration, etc.) cannot be quantified any longer. However, as we know today that characteristic packing properties depend sensitively on the above-mentioned quantities, see e.g. [8, 9]; results from previous investigations might be masked by these effects.

Since the experiments from Benenati and Brosilow [10] and Ridgway and Tarbuck [11] it is known that the packing structure in finite containers is not homogeneous: in wall zones the packing is structured whereas farther away in the bulk zone, generally, a random packing exists. For the latter, packing fractions are close to the value for random close packing,  $\gamma_{\text{RCP}} \approx 0.64$ , determined first by Scott [12]. Based on experiments with cylindrical containers with loosely filled or moderately densified monosized sphere packings [10, 11, 13], a wall zone thickness of 4–5 sphere diameters  $d$  was found. This value is still the basis of several void fluctuation correlations, compare for example [14]. However, Owe Berg et al. [15] and Vanel et al. [16] showed for monosized sphere systems that structured packings can occupy almost the total packing volume of cylindrical containers for  $D/d \gg 1$ , or  $H/d \gg 1$  (where  $D$  is the cylinder diameter and  $H$  is the container height). In detailed X-ray tomography experiments with defined one-dimensional (1d) vibration, Reimann et al. [17] recently observed largely ordered structures for a variety of container/sphere diameter parameters.

Packing fractions in well structured zones are significantly larger than  $\gamma_{\text{RCP}}$ . However, the container packing fraction,  $\gamma_t$ , does not indicate clearly if structured packings play an essential role because, depending on the container

† Deceased on May 25, 2018

geometry, the packing fractions in the wall layers of  $d/2$  thickness,  $\gamma_{d/2}$ , can decrease  $\gamma_t$  considerably, see Section 3.1. Packing fractions significantly larger than  $\gamma_{RCP}$  were experimentally obtained in cylindrical containers by [17–19] as well by Dai et al. [20] with discrete element modeling, DEM, simulations for containers with  $D/H < 1$ . The hexagonal structure grew upwards from the plane bottom wall and finally dominated the total packing volume.

With the availability of X-ray computed tomography (CT) as well as the progress achieved in the development of numerical simulation methods (e.g., DEM), packing structures can be studied in much more detail by determining particle positions, contact number and contact angle [6, 17, 21, 22] distributions and even contact surface sizes [22, 23]. The degree of order has been quantified by various mathematical tools [24–26]. A combination of CT with DEM was proposed by Delaney et al. [27], where small displacement perturbations using DEM were used to compensate the CT measurement errors.

Previous CT investigations concentrated on the use of both circular containers and monosized spheres. Results for binary and polydisperse sphere packings were reported by Scaffidi-Argentina et al. [28] and Al-Raoush and Alsaleh [29], respectively.

DEM simulations have been performed for all kinds of spherical systems and for non-spherical particles as well [30–34]. Most of these investigations do not include wall effects. In respect to our investigations, the differences between monosized and polydisperse sphere packings are of special interest. Compared to monosized systems with  $\gamma_{RCP}$ , with increasing polydispersity, packing fractions increase and contact numbers decrease [2, 25, 35]. However, for a small polydispersity, of relevance in the present paper, differences to monosized systems are negligible. With respect to compressed sphere packings, polydisperse packings result in larger volumetric strains for the same initial packing fraction [2, 36], caused by the larger particle mobility. This result might be of relevance with respect to the susceptibility to granular convection flow.

Compared to circular containers, investigations with prismatic containers are less numerous although such containers are relevant for many technical applications, among others for blankets in future nuclear fusion reactors [3, 14, 37]. In the latter case, slender prismatic containers are of interest where one dimension is significantly smaller compared to the other dimensions, that is  $X \ll Y = Z$ , compare Fig. 1. With decreasing  $X/d$ , wall zone effects become increasingly important, however, the influence of the parameter  $X/d$  on  $\gamma_t$  is much less known than the parameter  $D/d$  for cylindrical containers.

Packing experiments with mono-sized and polydisperse spheres have been carried out, e.g. by [38–40], without accessing the internal packing structures. For fusion reactor blankets [3, 37, 38], the containers are closed apart from a small filling opening, (FO). For efficient filling/vibration, the FO must be at the highest elevation [38, 41] which hinders obtaining a homogenous packing in the total container as measured by [41]. The recent DEM simulations performed by Desu et al. [42] are of significant relevance for the work reported in this paper: a cubic container with a free surface was investigated with dimensions of  $25d$ , filled by gravity without or with  $(1d)$  horizontal vibration. With lateral vibration, it is found that the wall zones are signifi-

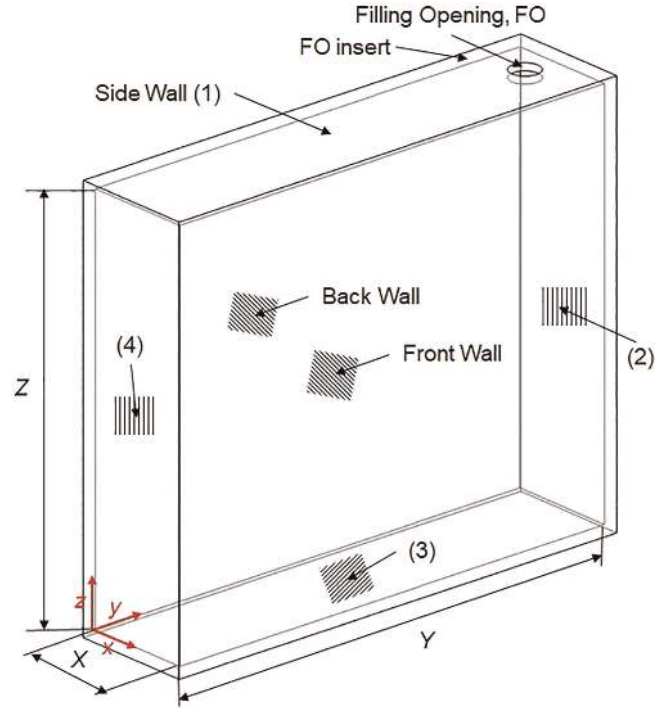


Fig. 1. Sketch of the prismatic containers with Cartesian coordinate system and denominations of different walls. During vibration, the filling opening (FO) is at the highest elevation.

cantly increased from the initial thicknesses of  $5-6d$ , and  $\gamma_t$  increases from 0.62 to 0.64. Results are also given for additional uniaxial compression of the packings. This results for the non-vibrated packing in a  $\gamma_t$  increase 0.64; for the initially vibrated packing,  $\gamma_t$  becomes 0.65. Connected to the increase of  $\gamma_t$  is the strong increase of highly ordered fcc and hcp zones.

In the present article, first detailed CT results are reported for a polydisperse sphere system, experiment “Exp (P)”. The fact that a prismatic container is used might be marginally restrictive for the conclusions of the results in respect to cylindrical containers. First detailed CT results for prismatic containers filled with monosized spheres, experiment “Exp (M)”, will be also presented and it will be demonstrated that significant differences exist compared to cylindrical containers.

## 2. Experiments

### 2.1. Container and packing specification

Figure 1 shows a schematic diagram of the Plexiglas container. The container dimensions were selected to fit the tomography experimental requirements, see Section 2.2. Nominal dimensions in the  $x$ ,  $y$ ,  $z$  directions are  $X = 20$  mm and  $Y = Z = 80$  mm; the real dimensions of the two containers differed marginally from these values. The containers are considered as slender containers because of the quite small  $X/d$  values.

Figure 1 also contains the denominations for the various walls: the large front and back walls in the  $y-z$  planes and the smaller side walls (1)–(4). The containers were filled through an opening at the highest elevation by different

methods: a) the container was fixed on the horizontal table of the 1d vibrating device (Renfert Vibrax REF 1830000) in a position revolved round the horizontal by about  $45^\circ$  and then vibrated in the vertical direction; b) the container was mounted with the bottom side (3) on the vibrator table and the total system was fixed in a position revolved round by about  $45^\circ$  and then vibrated in a direction of about  $45^\circ$  to the vertical; c) (only for monosized spheres) the container was mounted with side wall (4) on the horizontal vibrator table and vibrated. After two fillings, the crystallized packing had such a stiffness that for further fillings/vibrations the system could be revolved in steps round the horizontal up to the final position of about  $45^\circ$ . It showed that with all the above mentioned filling procedures similar results were obtained. For (P) and (M), the arrangement a) was used.

Filling through the FO (diameter 5.5 mm) was only performed for the last steps for achieving complete filling. In the other cases, a 10 mm wide part of side wall (1), containing the FO, see Fig. 1, was removed.

In (M), aluminum spheres with a mean diameter of  $d = 2.31$  mm were used with  $d$  tolerances of about 2% and deviations from the roundness index ( $= 1$ ) below 1%, determined with a Leika QWin Suite (version 3.11) system. Although these spheres are not perfectly monosized, highly structured packings were obtained recently [17]. For (P), polydisperse  $\text{Al}_2\text{O}_3$  spheres with a quite narrow range of diameter spread were selected, being characteristic for many systems where in previous publications only a mean diameter was given, which could imply the use of spheres with a negligible diameter tolerance. The polydisperse spheres were generated by sieving with mesh sizes of 1.0 and 1.25 mm. Sieving cannot prevent the occurrence of some ellipsoidal or lentil-type particles. By rolling down an inclined plane probably most of these particles were sorted out. The mean diameter  $d$  was determined to  $d = 1.12$  mm; 98% of the particles are between 0.9 and 1.25 mm; the sphere fractions in this range are well fitted by  $N_{\text{sph}}/N_{\text{sph-total}} = -32.45 + 58.59d - 26.06d^2$ . In the following, the dispersity of the used system is characterized by the ratio of largest to smallest sphere diameters,  $\lambda = 1.39$ .

The containers were first filled to  $\approx 60\%$ , followed by 1d vibration with a defined vibration intensity  $\Gamma = a(2\pi f)^2/g$ , where  $a$ ,  $f$  and  $g$  are the amplitude of the pulsation, the vibration frequency and the gravitational acceleration, respectively. In the next step, the container was filled up to about 80% and vibrated. Then the residual empty space was completely filled and vibrated. This procedure was repeated until no further particles could be added. The final nominal packing fractions,  $\gamma_{t\text{-nom}}$ , were conventionally determined by weight and volume measurements.

For (P), the  $\Gamma$  values were selected such that convective granular flow was largely suppressed in order to avoid separation effects. However, even for  $\Gamma \approx 1$ , where an observable densification of the packing started, the occurrence of granular flow could not be excluded. This might be a characteristic feature of polydisperse packings where the development of ordered structures is significantly smaller compared to monosized packings. Only when the container was largely filled, could  $\Gamma$  be increased without the occurrence of granular convection but still enabling local particle relocation.

For (M), the situation was different: here,  $\Gamma \approx 2$  resulted in an initial granular convection, which came to rest with the formation of crystallization zones at the walls. Then,  $\Gamma$  could be increased without changes of the crystallized packing. This stable structure served as a template for the next filling/vibration step. This procedure was repeated with increased  $\Gamma$  until complete filling. In the final stages the maximum nominal vibrator intensity  $\Gamma \approx 6$  was applied, however, in these cases the particle movement amplitudes were restricted because of the nearly complete enclosure in the container; “amplitude limited vibration”, compare [17].

Table 1 shows experimental parameters for (M) and (P). Stimulated by the large  $\gamma_t$  obtained for (M), see Section 3.1, further filling experiments were performed with the container according to Fig. 1, however, with two more slightly differing  $X$  values. Additionally, a slender prismatic container with  $X = 10.1$  mm and  $Y = Z = 100$  mm was used, see Table 2. One experiment was performed with spheres from (P), for the others, monosized spheres with different diameters were used.

## 2.2. X-ray computed tomography and volume image analysis

In order to be able to study precisely morphological features of the experiments, volume images with excellent contrast as well as signal-to-noise ratio are required. Synchrotron radiation was therefore chosen, i. e. to acquire tomographic data sets using hard X-rays. Measurements were carried out using beamline ID19 of the European Synchrotron Radiation Facility (ESRF) in Grenoble, France. In order to access sufficiently high photon flux density at the required photon energy to transmit the comparable large samples, the beamline was operated in white mode with a wiggler (w150, gap 29) as source. The softer part of the radiation was filtered with 5.6 mm of aluminum, 8 mm of copper and 1 mm tungsten plus a 1 mm-thick diamond filter. The resulting spectrum is rather broad with a peak at

Table 1. Experimental parameters and packing fractions for Exp (M) and Exp (P).

Container dimensions: $X = 20$ mm, $Y = Z = 80$ mm								
Exp	$d_{\text{mean}}$ (mm)	$X/d$	$\gamma_{t\text{-nom}}$	$N_{\text{sp}}$	voxels/ $d$	$\gamma_{t\text{-CT}}$	$d_{\text{nom}}/d_{\text{CT}}$	$\gamma_{t\text{-nom}}/\gamma_{t\text{-CT}}$
(M)	2.312	8.6	0.677	12 361	79	0.682	0.98	0.992
(P)	1.117	18	0.624	105 044	37	0.624	1.03	1.0

Table 2. Prismatic container packing experiments.

$d$ (mm)	$X^*$ (mm)	$X/d$	$N_{lay}$	$s/d$	$\gamma_{t-meas}$	$\gamma_{t-est}$
2.00	20.0	10.0	11	0.800	0.655	0.714
2.00	20.7	10.4	12	0.330	0.680	0.715
2.31	20.0	8.7	10	0.271	0.677	0.700
2.31	20.7	9.0	10	0.581	0.657	0.701
2.31	21.7	9.4	11	0.089	0.672	0.701
4.00	20.0	5.0	5	0.720	0.628	0.689
4.00	21.7	5.4	6	0.325	0.646	0.691
5.00	20.0	4.0	4	0.540	0.620	0.677
5.00	21.7	4.3	5	0.060	0.645	0.680
1.0–1.25	20.0	18.0			0.624	0.626
$d$ (mm)	$X^{**}$ (mm)	$X/d$	$N_{lay}$	$s/d$	$\gamma_{t-meas}$	$\gamma_{t-est}$
2.00	10.1	5.1	5	0.770	0.637	0.703
2.31	10.1	4.4	5	0.205	0.663	0.690
1.0–1.25	10.1	9.1			0.617	0.619

\*  $Y = Z = 80$  mm

\*\*  $Y = Z = 100$  mm

around 200 keV. Radiographic images of the specimens under different angles of view were recorded with an indirect detector: a 1 mm-thick LuAG:Ce (Ce-doped  $\text{Lu}_3\text{Al}_5\text{O}_{12}$ ) lens-coupled to the ESRF inhouse-developed CCD-camera FReLoN ( $2048 \times 2048$  pixel,  $14 \mu\text{m}$  pixel size). The corresponding pixel size is  $30 \mu\text{m}$ . Tomographic reconstruction was performed by standard filtered-back projection. Further details have been published previously [17, 43].

Subsequent volume images analysis was carried out using the iMorph software. Originally used to segment cellular materials such as open cell metal foams, iMorph uses a classical watershed method based on maximal ball markers to individualize the spheres and to make a precise contacts analysis [44, 45]. The binarization process that consists in identifying voxels belonging to spheres or void is obtained through a simple threshold applied to the gray level distribution of voxels. The incertitude in the arbitrary threshold (that we choose to obtain a packing fraction value close to the experimental one) is impacting the voxels located at the interface between solid and void. Figure 2 shows the gray level distributions of the (M) and (P) CT-images and the packing fraction curve (1 – normalized cumulative gray distribution curve). This error depends on the voxel size and on the total surface of the spheres. Thus, the error is more important for (P) as the spheres are smallest (high specific surface). One can quantify the error on the packing fraction values by taking different thresholds close to the selected ones. For (P), the selected threshold  $126 \pm 10$  gives a packing fraction  $0.624 \pm 0.012$ , and for (M) the threshold  $141 \pm 10$  gives a packing fraction equal to  $0.682 \pm 0.009$ , see Table 1.

Only one maximal ball can be located in a sphere. The maximal balls are obtained from the computation of the aperture map [46]. The aperture map is obtained from the distance map computation and contains for every solid voxel the radius of the maximal included balls that enclose the voxel.

The maximal balls centers are used as watershed markers that we used to label them, see Fig. 3. One can then com-

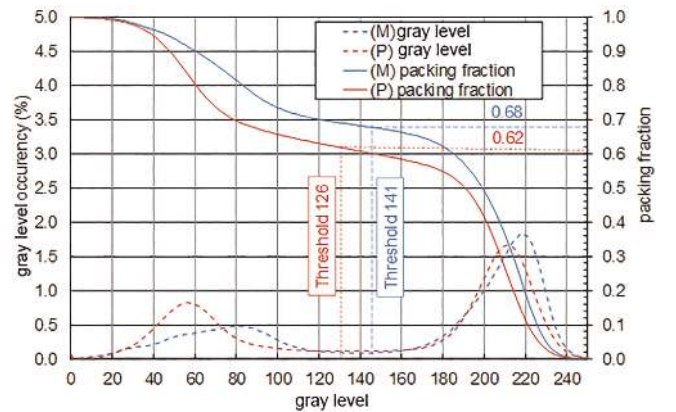


Fig. 2. Characteristic gray level distribution for XCT imaging and the corresponding dependence of the packing fraction  $\gamma_t$ .

pute the volume of every sphere to deduce the diameter of same volume spheres d-CT, as shown in Table 3, where  $\sigma$  is the standard deviation. We also computed the equivalent ellipsoid to obtain morphological information of each spheres to verify the sphericity of the balls. This allowed us to identify the half axis length that corresponds to the dimension of the balls along the different main axis of the equivalent ellipsoid. Thus, “ $a$ ” corresponds to the main dimension toward the main direction of the ellipsoid and  $a > b > c$ . We obtained good sphericity and also the computed diameters are in good agreement with nominal values, so this reinforces the arbitrary threshold that we chose to binarize the volumes.

The local packing fraction can be computed for every segmented ball by computing the local Voronoi cells and dividing the ball volume by the Voronoi cell. We compute directly the Voronoi map by using the same watershed algorithm and instead of taking the maximal ball center as marker, we use the entire labialized balls as markers. Then every sphere is totally encapsulated into its Voronoi cells and the local packing fraction is inferior to 1, see Section 3.6.

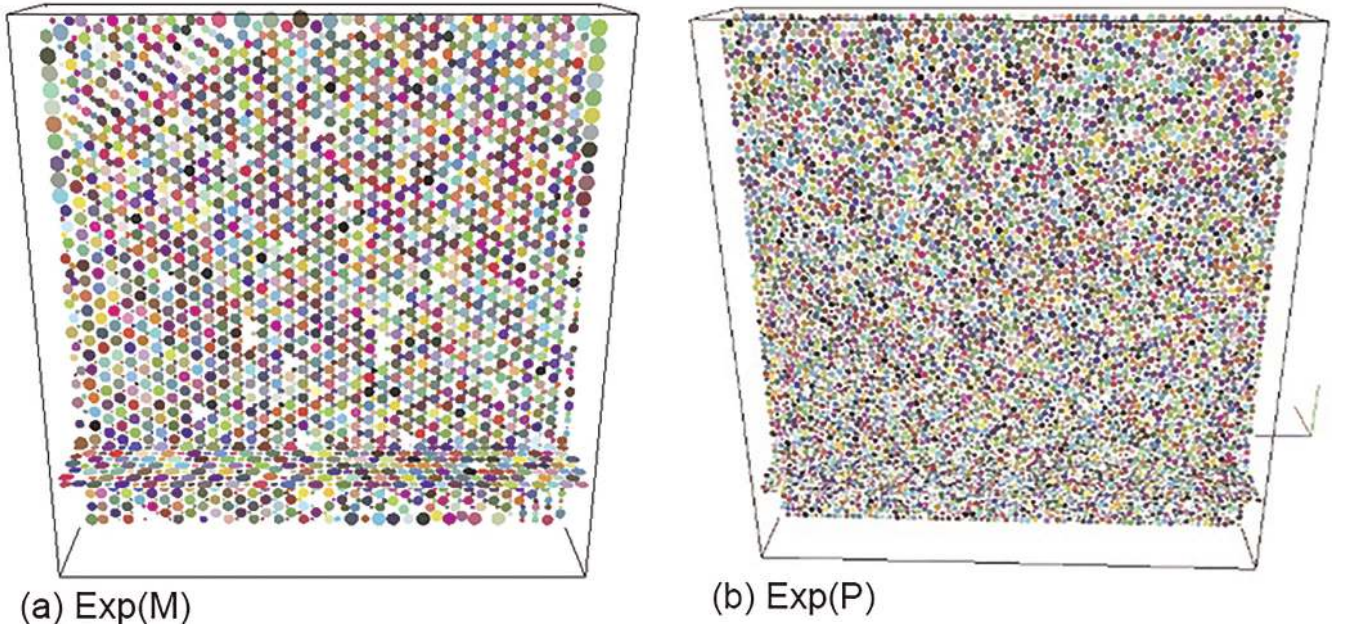


Fig. 3. Volume rendering of particles in the prismatic containers: (a) Exp (M) with  $\approx 12440$  spheres; (b) Exp (P) with  $\approx 105000$  spherical particles. Colors are for marking purpose only.

Table 3. X-ray image sphere analysis. All measures are reported in mm.

Exp	$d_{CT}$	$\sigma$	Half axis $a$	$\sigma$	Half axis $b$	$\sigma$	Half axis $c$	$\sigma$	Aperture radius	$\sigma$
(M)	2.367	0.01	1.065	0.005	1.059	0.004	1.056	0.005	1.097	0.056
(P)	1.086	0.06	0.511	0.034	0.494	0.026	0.484	0.027	0.484	0.049

### 3. Results and discussion

#### 3.1. Packing fractions

Table 1 shows packing fraction comparisons between nominal and CT values. The  $\gamma_{t-nom}$  and  $\gamma_{t-CT}$  values agree well, deviations between the mean diameters are less than 2%. For (M),  $\gamma_t$  is surprisingly large considering the small value of  $X/d$ . For circular containers, various correlations describe the  $\gamma_t$  decrease with decreasing  $D/d$ , see e. g. Scott [12] and Zou and Yu [47], and significantly lower  $\gamma_t$  values are reported for the cases with comparable values of  $D/d$ , even for 3d vibration and layer-wise filling [19]. Table 2 contains the results for all packing experiments; here, the nominal  $d$  values were used for (M) and (P).

With monosized spheres, homogeneous structures in the slender prismatic containers are preferentially formed at the large front and back walls ( $y$ - $z$  walls), and crystallization proceeds in the  $x$ -direction, details in Sections 3.2 and 3.3. For dense hexagonal packings, sphere layer distances are  $0.817d$  and the wall distances to the  $y$ - $z$  walls are  $0.5d$ .

The number of layers can then be calculated by

$$N_{lay} = \text{INT}((X - d)/(0.817d) + 1) \quad (1)$$

and the dimensionless gap  $s/d$  which exists if the ideal hexagonal structure differs from the width  $X$ , is given by

$$s/d = X - (N_{lay} - 1) 0.817 - 1 \quad (2)$$

It was observed that for larger  $s/d$  values, zones with differently orientated structures are at the  $y$ - $z$  walls occurred, as well as less ordered structures at the side walls. Table 2 shows that large  $\gamma_t$  values are obtained preferentially for small  $s/d$ . Most pronounced is this for  $d = 2.31$  mm in the container with  $X = 10.1$  mm: for a  $X/d$  of less than 5,  $\gamma_t > 0.66$  was obtained.

Table 2 also contains the column with estimated packing fractions,  $\gamma_{t-est}$ . In this assessment, first used in previous work [47], the total volume  $V_t$  is divided into an inner volume,  $V_{t-in}$  and the volumes of all  $d/2$  layers,  $\Sigma V_{d/2}$ . Then, it holds that

$$\gamma_t \leq \gamma_{t-est} = (\gamma_{t-in} V_{t-in} + \Sigma \gamma_{d/2} V_{d/2}) / V_t \quad (3)$$

where  $\gamma_{d/2}$  is the packing fraction of an individual  $d/2$  wall layer. The  $\gamma_{d/2}$  values can be evaluated with the wall minima of the void distributions,  $\varepsilon_{min}$ , see Section 3.3, by

$$\gamma_{d/2} = 0.604(1 - \varepsilon_{min}) / 0.907 \quad (4)$$

In Eq. (3), for monosized spheres the values for hexagonal dense packing are used with  $\gamma_{t-in} = 0.74$  for the inner volume and  $\gamma_{d/2} = 0.604$  for the  $y$ - $z$  wall layers. For all side wall layers,  $\gamma_{d/2} = 0.302$  is assumed because ideally, only every second sphere is in contact with these walls, see Section 3.3. The  $\gamma_{t-est}$  values are an upper bound because the gaps, mentioned above, are not considered in this estimation.

The reason for large packing fractions in prismatic containers is that crystallization can proceed less restrictedly from plane walls compared to cylindrical containers. At cylindrical walls, a fairly well structured hexagonal pattern can be also obtained by appropriate vibration. However, because of the smaller diameter of the second layer where the sphere centers are located, the second layer spheres can no longer arrange well in the dips of the first layer spheres; this “curvature effect” was discussed in detail by [17]. For cylindrical packings with large  $D/d$ , this effect is less expressed close to the cylindrical wall, however, still a non-structured packing occurs further away.

In slender prismatic containers, crystallization on the large walls dominates the total packing volume, see Section 3.3. With increasing  $X/d$ , it becomes more difficult to obtain only one type of structure in the packing volume. Crystallization zones originating from different walls compete and differently orientated structures occur. In the boundary regions, the spheres are arranged less ordered, which decreases  $\gamma_t$ . Such structures were determined by Desu et al. [42] with DEM simulations for a cubic container, applying horizontal vibration. One can speculate if by vertical vibration and optimized vibration parameters packing fractions significantly above 0.64 could have been achieved also for this container geometry.

For (P),  $\gamma_{t-est}$  is determined with the individual  $d/2$  packing fractions taken from the void fraction distributions. For the  $y$ - $z$  walls;  $\gamma_{d/2} = 0.5$ , and for the side walls;  $\gamma_{d/2} = 0.47$ . For the bulk, the value measured for the container with  $X = 20$  mm is taken,  $\gamma_{t-in} = 0.638$ . Table 2 shows that there is a good agreement with the measured data for the container with  $X = 10.1$  mm.

In (P), the value  $X/d \approx 18$  is large compared to the thicknesses of structured wall zones and with this, differences to cylindrical containers with similar  $D/d$  values are expected to be small. For slender prismatic containers with considerably smaller  $X/d$ , the random packing in the bulk disappears and the wall zones become interconnected. This could promote the development of regular structures and could result in a different dependence  $\gamma_t = f(X/d)$  compared to  $\gamma_t = f(D/d)$  for circular cylinders. A corresponding result was observed by Reimann et al. [40].

### 3.2. Void fraction distributions

Figure 4 shows void fraction distributions (VDs) in the direction of the  $x$ ,  $y$  and  $z$  axis, evaluated with the total packing volume. In (M), strong fluctuations exist in the total volume. This is most clearly seen in the VDs in  $x$ -direction, Fig. 4b. Here, no damping effect is observed and each wave

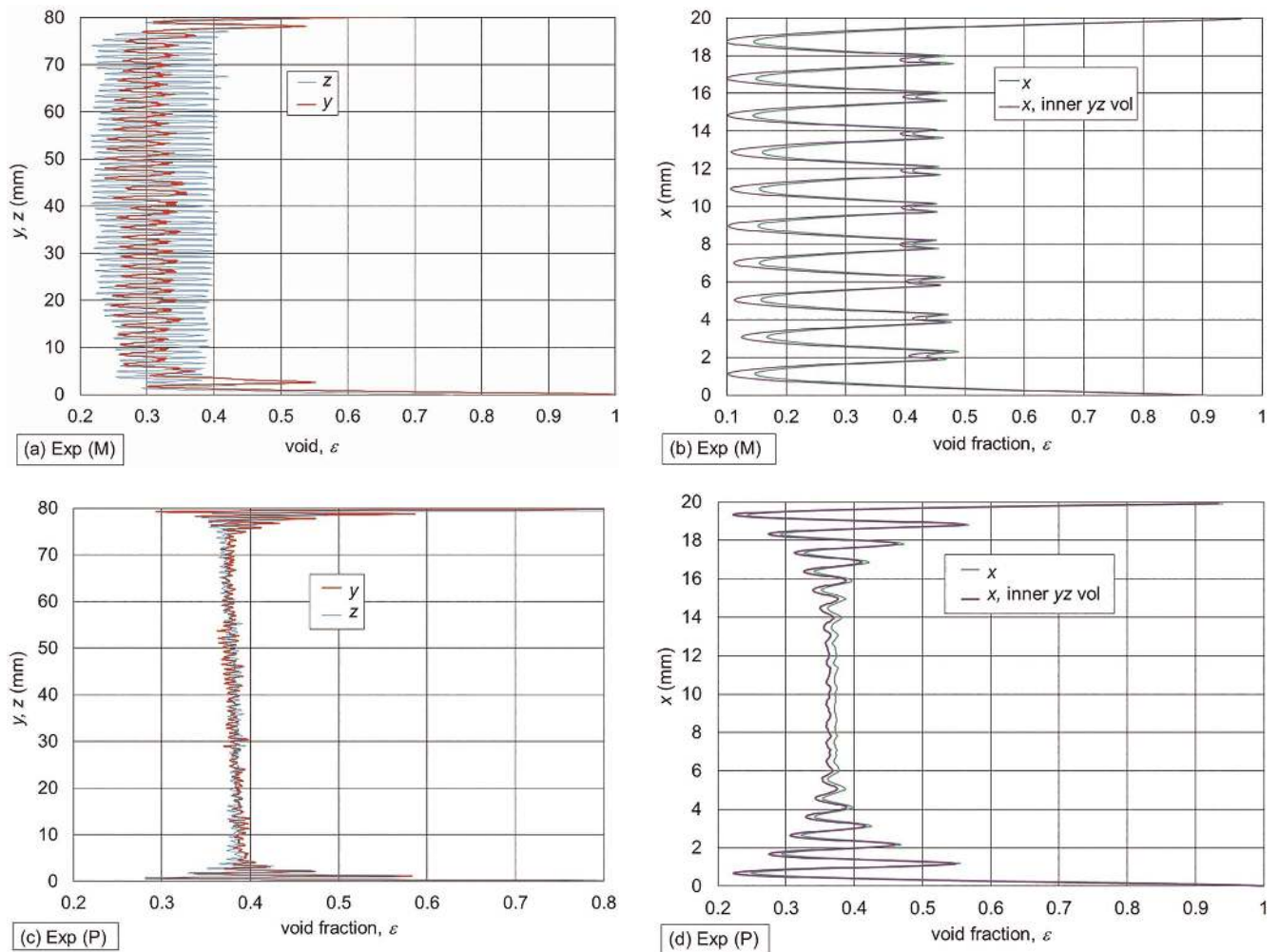


Fig. 4. Void distributions (VDs) for (M) and (P): (a) and (c): VDs in the  $y$  and  $z$  directions; (b) and (d): VDs in the  $x$ -direction. Fluctuations are characteristic for structured packing; in (M) these fluctuations exist in the total container volume whereas for (P) fluctuations are restricted to wall zones.

has double peaked maxima caused by the joint zone of two neighbored sphere layers, characteristic for dense sphere packings, measured first by [17] in an experiment with an even larger relevant  $X/d$ . In Fig. 4a, the VDs in the  $y$  and  $z$  direction are presented. Here, surprisingly, the first wall minima have larger void fraction values than the following minima. This behavior has not been observed before. The explanation is given in Section 3.3.

For (P), the wall zone fluctuations are most developed in the  $x$ -direction and damp out after 4–5 wavelengths; a bulk zone with random packing exists in between. The VDs of (P) in the  $y$  and  $z$ -directions contain a large zone with non-structured packing, a remarkable gradient is observed in the  $z$ -direction; in the  $y$ -direction this effect is smaller. Void fraction gradients indicate nonhomogeneous packing distributions, see Section 3.6.

Wall structure details are better elaborated by using characteristic inner volumes, compare [17], for which not relevant wall zones are cut-off. For the VD in the  $x$ -direction, wall zones with thicknesses of 5 mm at the side walls (1)–(4) were cut-off, resulting in an  $y$ – $z$  cross-section with  $5 \text{ mm} < y, z < 75 \text{ mm}$ . This inner  $y$ – $z$  volume is considered to be characteristic for two infinitely large parallel plates with a distance of 20 mm.

For (M), the VD for the inner  $y$ – $z$  volume has minima very close to the value for hexagonal dense packings,  $\varepsilon_{\text{hex}} = 0.093$ , which corresponds to a wall coverage of 0.907. Again using the values for hexagonal dense packings, see Section 3.1, a packing fraction of  $\gamma_{\text{hex}} = 0.724$  is obtained which is close to the measured value  $\gamma_{\text{CT}} = 0.714$ .

For (P), the void fluctuations for the inner  $y$ – $z$  volume are also more developed and in the bulk zone a lower mean void fraction is obtained with  $\varepsilon_{\text{bulk}} = 0.362$ , corresponding to  $\gamma_{\text{bulk}} = 0.638$ , being very close to  $\gamma_{\text{RCP}} \approx 0.64$  for monosized spheres. For the small polydispersity of  $\lambda = 1.39$ , the difference to monosized spheres is negligible.

Figure 5 shows for the inner  $y$ – $z$  volume both packing fraction and sphere number distributions as a function of  $x^* = x/d$ : In (M), the distances between all layers are close to the value for hexagonal dense packing,  $\Delta x^* = 0.817$ .

### 3.3. Sphere distributions in wall layers and bulk

Figure 6 shows for (M) views on the front wall obtained by CT and photography. In the CT figure, the positions of the sphere centers of the wall layer are plotted as circles which have about the same size as the spheres. The agreement is obvious; especially comparing structural imperfections (indicated in red). An almost perfect hexagonal pattern at the total front wall is observed in contrast to the DEM predictions [42] resulting in ordered wall zones with different orientations.

Such CT figures provide pivotal insights for understanding for (M) the unexpected  $y$  and  $z$  VDs in Fig. 4a. Figure 7 shows that for the bottom side wall (3) the coverage of the first wall layer with sphere centers at  $z^* = z/d = 0.5$  is quite small. Showing also the sphere centers of the second layer, located at about  $z^* = 1$ , it is obvious that many spheres fit quite well into the dips. The reason is the dominant structure on the large front and back wall consisting in Fig. 6 of “vertical sphere chains”. Ideally, every second vertical row of this wall layer has a sphere in contact with the side wall (3), the lowest spheres of the other rows are located at

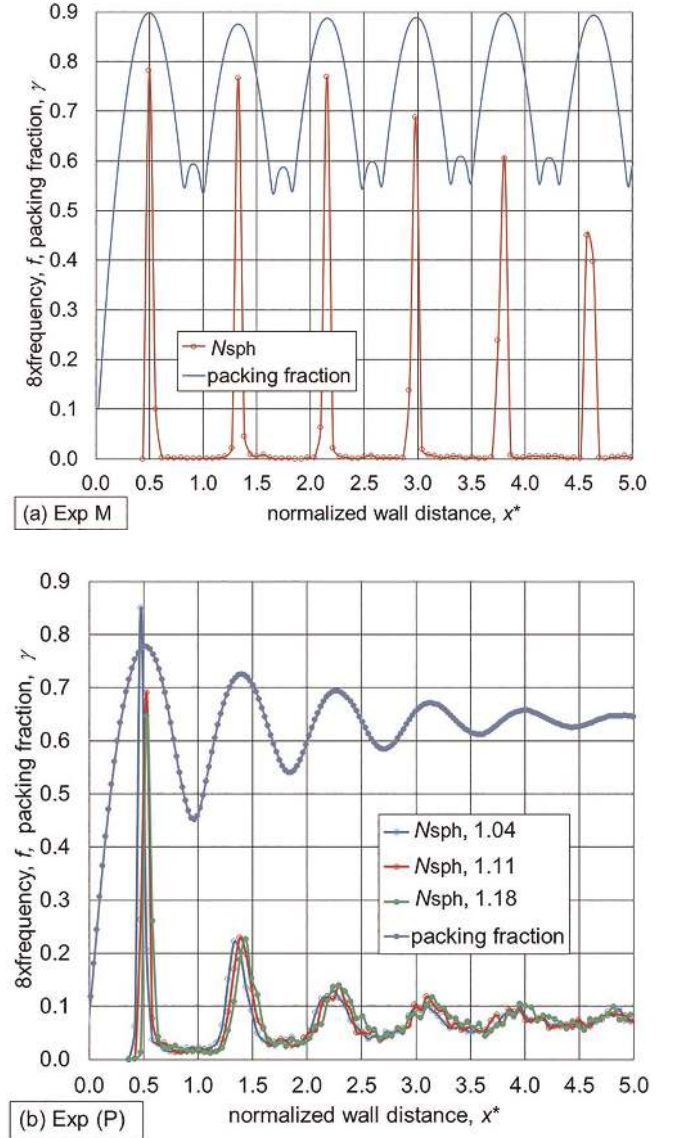


Fig. 5. Packing fraction and sphere number distributions in the normalized  $x$  direction for the inner  $y$ – $z$  volume. Compared to (M), a significant damping of the fluctuations is observed for (P) relevant for the decrease of structured ordering with increasing wall distance.

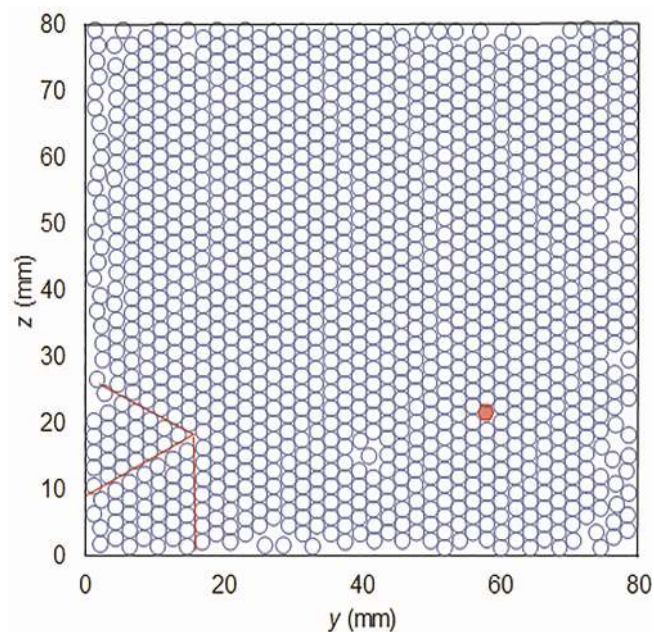
$z^* = 1$ , see Fig. 6. Ideally, this is also the case for every layer in the  $x$ -direction. The resulting pattern is well developed in the left part of Fig. 7. Because this situation at the bottom wall is unstable with respect to gravity, this pattern is easily disturbed and more spheres are in contact with the wall. In the  $z$ -direction the layers have a distance of  $\Delta z^* = 0.5$  compared with 0.817 in the  $x$ -direction, which can be verified by the different fluctuation frequencies in Fig. 4. At the side walls (2) and (4), ideally, vertical sphere chains should exist with again every second row in contact with the walls; the other rows should be staggered by the distance  $\Delta y^* = 0.866$ . Again, this different frequency can be detected in Fig. 4. The righthand side of Fig. 7 shows this structure partly for side wall (4). It should be mentioned that “vertical sphere chains” are not mandatory for the large order of the packing. In repetition experiments, also “horizontal sphere chains” were observed, with all spheres of the lowest horizontal row at the front wall are in contact

with the bottom side wall (3). Then, the lowest row of the layer behind is located at  $z^* = 1$ .

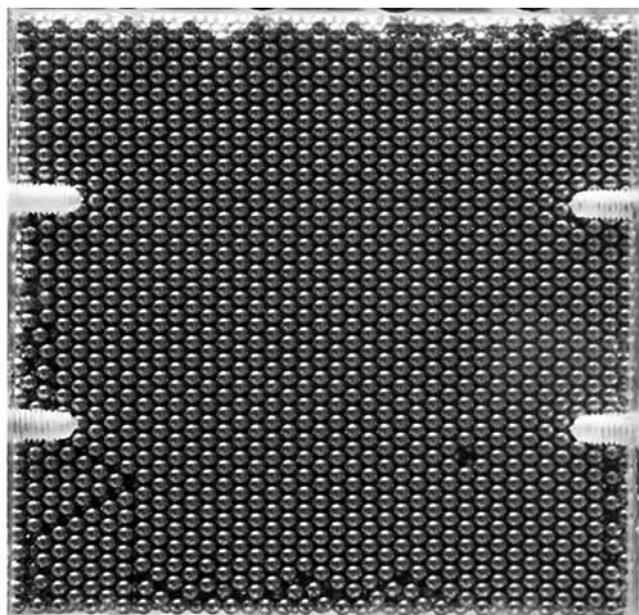
The fact that vertical vibration can result in structures where a part of the bottom spheres is fixed with defined distances apart from the wall was measured first in the present experiments. With the argument of gravitational instability, this situation was excluded, e.g. by McGeary [7], and the “double nested” structure was proposed where all wall layer spheres are in contact with the walls. (This double-nested structure was never observed in our CT experiments). Mandatory for obtaining the sphere structure of

(M) are probably small  $X/d$  values and an efficient vibration method. There are technical applications where such structures would be very beneficial [3, 37].

Figure 8 contains views on the front wall for (P). In the CT plot, the total number of spheres was divided into three fractions of 1/3 resulting in mean diameters of 1.04; 1.11, and 1.18 mm. It shows that the  $d$ -groups are not homogeneously distributed but are rather concentrated in clusters.

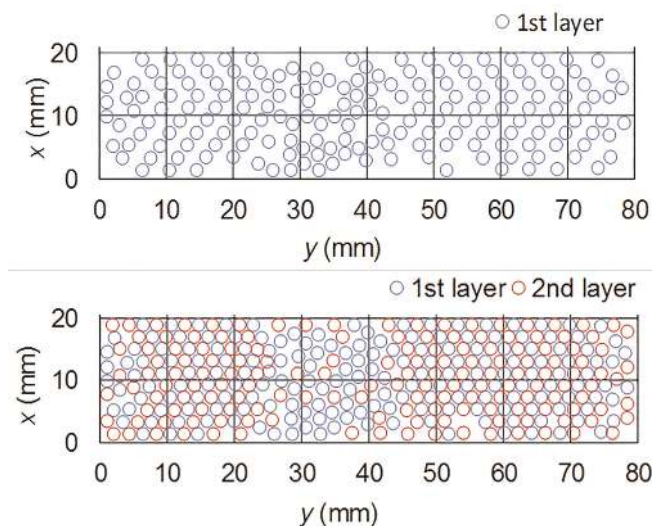


(a)

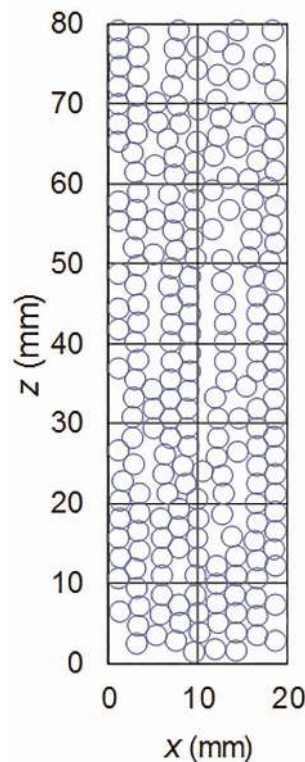


(b)

Fig. 6. Visualization of 1<sup>st</sup> wall layer in  $y$ - $z$  plane for (M): (a) CT results; (b) photography. Perfect hexagonal patterns are observed and a few disturbances (indicated by red in (a)).



(a)



(b)

Fig. 7. Visualization of sphere distributions in wall layers for (M): (a) side wall (3); blue symbols: 1<sup>st</sup> layer; red symbols: 2<sup>nd</sup> layer. (b) 1<sup>st</sup> layer on side wall (4). Characteristic are the small sphere coverages in the wall layers compared to dense packings at the front and back walls, compare Fig. 6.

Concerning the role of polydispersity on crystallization, there are CT results from three other experiments available (details are the subject of a future paper), performed with cylindrical containers: the first one is for a polydisperse system ( $\lambda = 1.5$ ); the other two are for binary systems with  $\lambda = 1.25$  and  $1.33$ . It is important to note that filling and vibration were the same as in [17] where for monosized spheres large well-developed crystallization zones were found. The important result is that the sphere distributions at the cylindrical walls are similar to those in Fig. 8, that is, significant hexagonal arrays do not exist and, therefore,

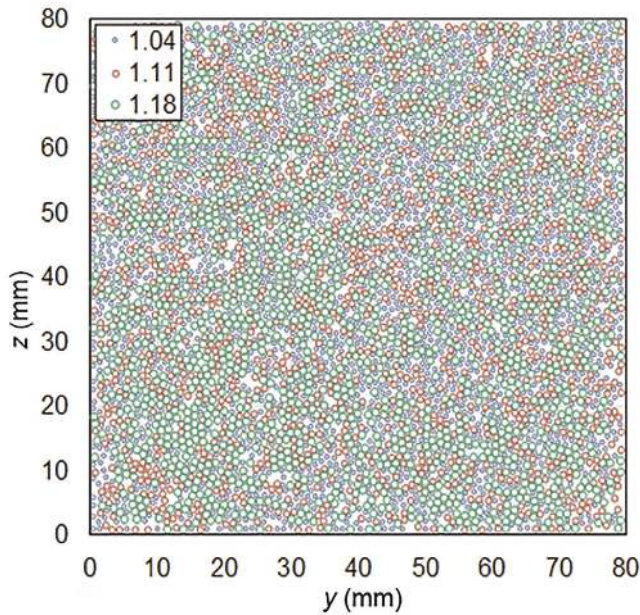
cannot serve as templates for further crystallization. Void fraction fluctuations disappear after wall distances of a few  $d$ , even faster than in (P).

Sphere distributions in the 1<sup>st</sup> and 3<sup>rd</sup> layers on the side wall 4 are shown in Fig. 9. The nonhomogeneous distribution in the  $x$ - $z$  plane is largest in the 1<sup>st</sup> layer and moderate in the 3<sup>rd</sup> layer.

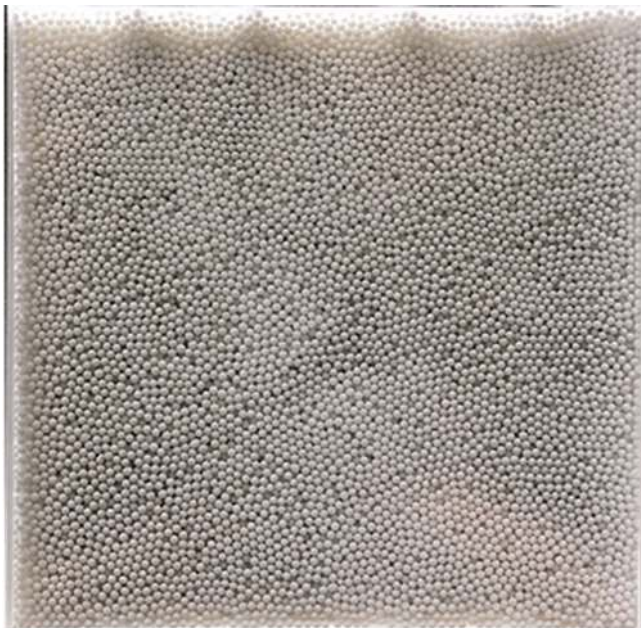
Table 4 summarizes the diameter fractions for the different wall layers and the bulk region. Generally, the small diameter sphere fraction is largest at the walls, see also Fig. 5, due to the arching effect described by Duran et al. [48]. This separation effect is most expressed for the side walls (3) and (4) which represent bottom walls during vibration in contrast to the top side walls (1) and (2), respectively. Sphere numbers are also larger above bottom plates compared to the spheres below top plates. The latter results in the large value of the first minima in the  $z$ -VD, see Fig. 4. For the total bulk volume, the fractions of the different sphere groups are about equal, however, segregation results in significant differences in subvolumes, see Section 3.6.

### 3.4. Coordination numbers

Only contacts between spheres are considered because contacts with the Plexiglas walls are not measured by CT. For dense hexagonal packing,  $N_c = 12$ , except for the 1<sup>st</sup> layer, where  $N_c = 9$ . Figure 10 again confirms the hexagonal structure in (M). (Note: The term dense hexagonal packing comprises hexagonal close packed, hcp, structures (AB packing sequence), face centered cubic, fcc, structures



(a)



(b)

Fig. 8. Visualization of 1<sup>st</sup> wall layer in  $y$ - $z$  plane for (P): (a) CT results; (b) photography. Compared to (M), the regularity is much smaller. Islands of spheres with similar sizes are observed in (a).

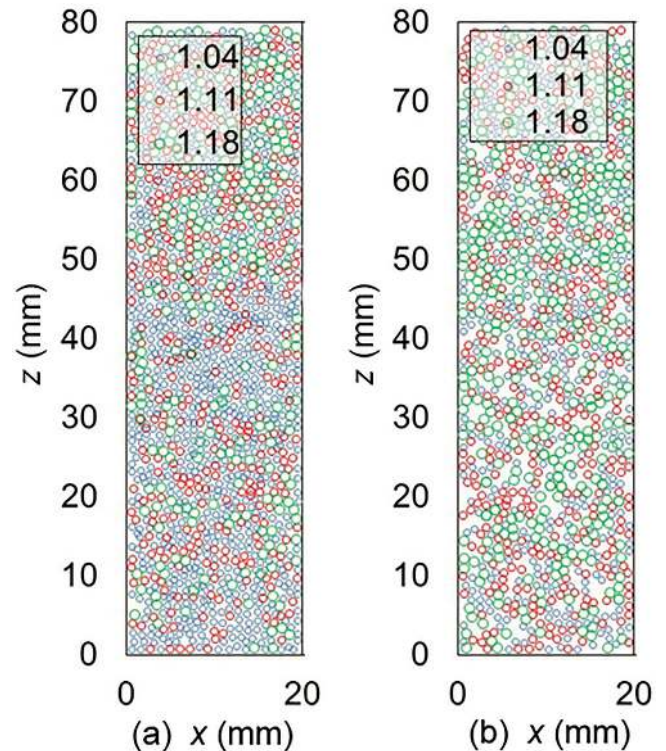


Fig. 9. Sphere distributions in (a) the 1<sup>st</sup> wall layer, (b) the 3<sup>rd</sup> wall layer of side wall (4) for (P): Characteristic for all side walls is the non-homogeneity of the sphere size distribution is largest in the 1<sup>st</sup> wall layers.

Table 4. Exp (P): sphere numbers,  $N_{\text{sph}}$  and  $N_{\text{sph}}$  fractions in first wall layers and bulk zone. (in total packing volume:  $N_{\text{sph}}$  fraction of each  $d$ -group =  $1/3$ ).

walls		S1	S2	S3	S4	front	back	bulk
$N_{\text{sph}}$	105042	1134	1174	1199	1276	5064	5051	48263
$d$ -group			$N_{\text{sph}}$	fractions				
1.05	0.333	0.379	0.360	0.581	0.542	0.352	0.350	0.327
1.11	0.333	0.315	0.327	0.293	0.279	0.341	0.332	0.335
1.18	0.333	0.306	0.314	0.126	0.179	0.308	0.317	0.338

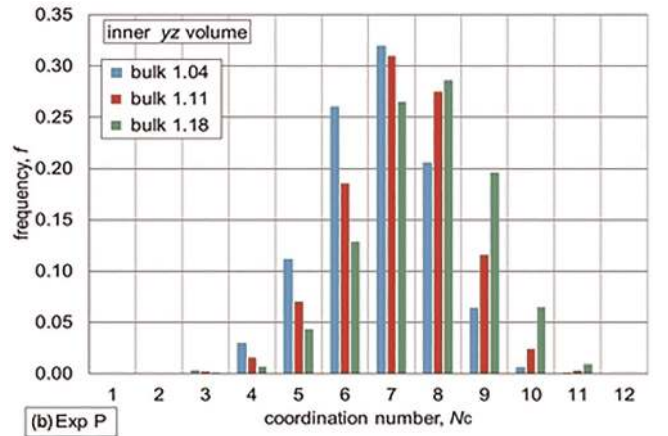
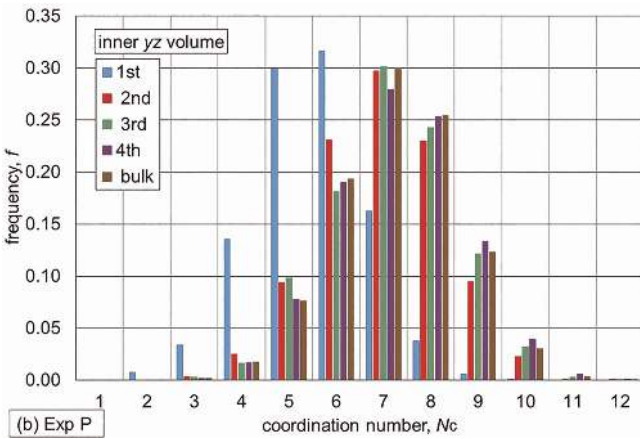
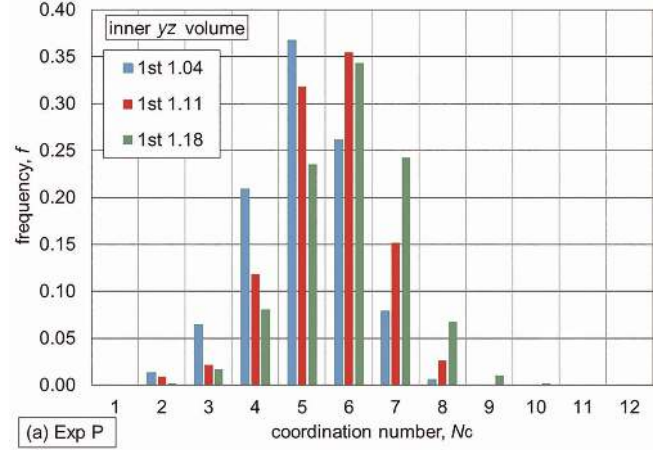
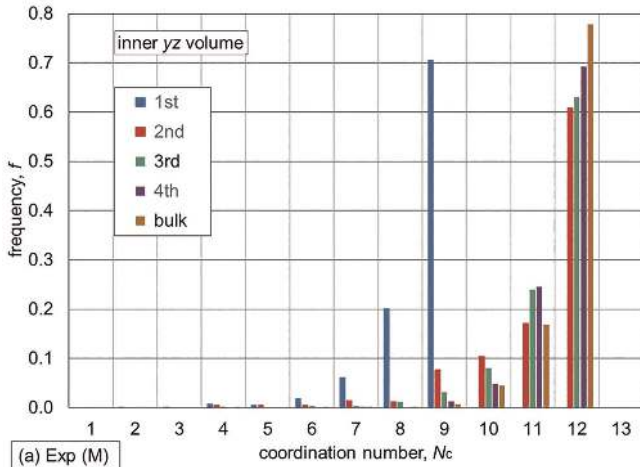


Fig. 10. Contact number ( $N_c$ ) distributions for different wall layers and the bulk zone (inner  $y-z$  volume): (a) In (M),  $N_c = 12$  is dominating for all cases except the 1<sup>st</sup> wall layer where  $N_c$  can not exceed 9. (b) In (P), broad distributions with a mean value of  $N_c \approx 7$  are found, except again for the 1<sup>st</sup> layer where  $N_c$  must be smaller.

Fig. 11. Exp (P): Contact numbers for different  $d$ -groups for (P) (inner  $y-z$  volume):  $N_c$  increases with  $d$  both in (a) the 1<sup>st</sup> wall layer, and (b) the bulk zone.

(ABC sequence) as well as arbitrary sequences, for details, see [17]).

For random close packing of monosized spheres, the mean value for the bulk zone is  $N_c \approx 7$  [24]. Figure 10 shows that this value is also measured, as expected for the small polydispersity of (P).

The dependence of  $N_c$  on the sphere diameter is more sensitively depicted by presenting the  $N_c$  distributions for the different  $d$ -groups, Fig. 11:  $N_c$  increases with  $d$  both in the bulk zone and the 1<sup>st</sup> wall layer. The  $N_c$  distribution for all  $d$ -groups results then in a broader distribution compared

to monosized spheres without changing remarkably the mean value which is consistent with the CT result from Al-Raoush [29].

### 3.5. Contact angle distributions

Regular structures are also reflected in the distributions of the angles between the contact points on the spheres. In the following figures, the poloidal angle  $\delta$  starts at the North Pole, the azimuthal angle  $\psi$  starts at the  $x$ -axis, and frequencies  $f$  for  $10^\circ$  groups are calculated. Again, results for the inner  $y-z$  volume are presented. For (M),  $\delta$  has characteristic

peaks at 0, 60, 90, 120, and 180°, Fig. 12, as expected for the sphere array shown in Fig. 6. This distribution is the same for all layers and the bulk zone, consistent for a regular structure in the total packing volume. The  $\psi$  distributions have peaks at 90 and 270° from contacts between spheres in the same layer and further characteristic peaks from contacts with neighbored layers. The  $\psi$  distribution is less regular compared to the  $\delta$  distribution because the  $\psi$  evaluation becomes less accurate for  $\delta$  values close to 90 and 180°.

For (P), specific peaks are most expressed for the 1st layer, Fig. 13. With increasing layer number, these peaks become rapidly smaller and a fairly homogeneous distribution is obtained. A significant dependence of the contact angles on the  $d$ -groups was not found.

### 3.6. Voronoi packing fractions

In Fig. 14, Voronoi packing fractions  $\gamma_{\text{Vor}}$  for the bulk volume are presented for three experiments. For (M), there is, as expected, a large peak at  $\gamma_{\text{Vor}} \approx 0.74$ . Surprisingly, a small peak at  $\gamma_{\text{Vor}} \approx 0.68$  exists as well. It showed that the latter values are located in a rather small zone close to the plane defined by the edges between the side walls (2) + (3)

and (4) + (1). During vibration this plane is about horizontal. Although the spheres crystallize preferentially at the front and back plates, the side plates might have a certain influence resulting in internal disturbances.

The distribution for (P) is compared with results for the bulk zone with random packing from “Exp A” [17], per-

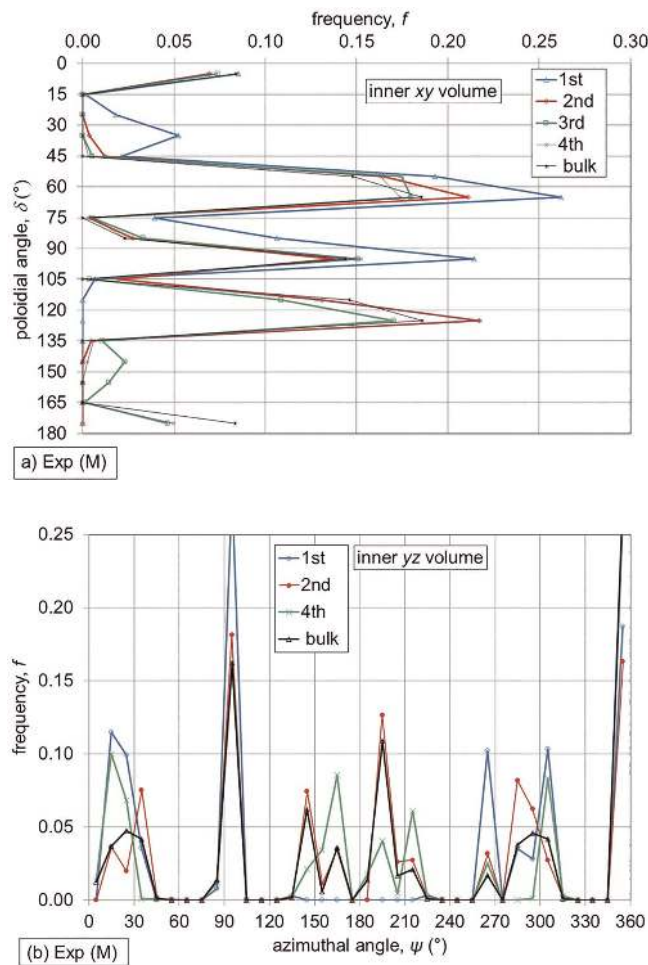


Fig. 12. Exp (M): Contact angle distributions for different wall layers (inner  $y$ - $z$  volume): (a) Both the poloidal angle  $\delta$ ; and (b) the azimuthal angle,  $\psi$ , have peaks at values in the total volume at values characteristic for dense hexagonal packing.

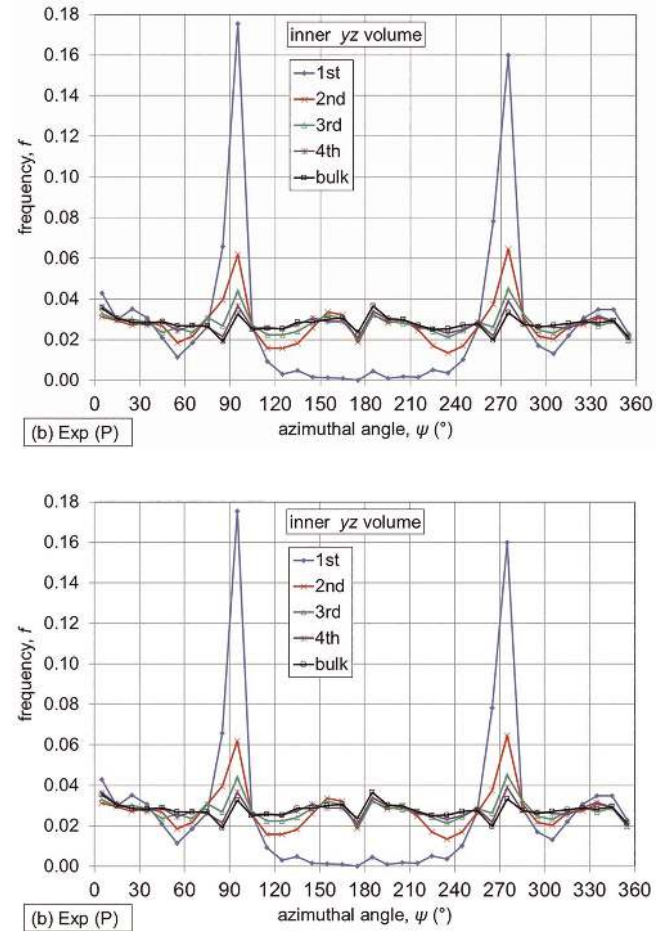


Fig. 13. Exp (P): Contact angle distributions for different wall layers (inner  $y$ - $z$  volume); (a): poloidal angle  $\delta$ ; (b): azimuthal angle,  $\psi$ . Distinct peaks are limited to small wall zones.

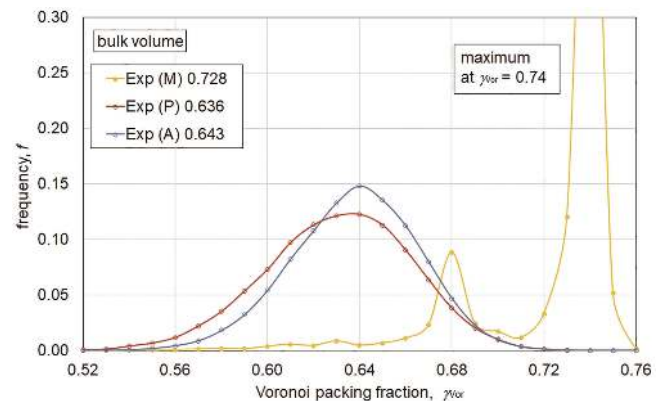


Fig. 14. Voronoi packing fraction  $\gamma_{\text{Vor}}$  distributions in bulk zone. In (M),  $\gamma_{\text{Vor}}$  has a large peak at 0.74, characteristic for dense hexagonal packing. The small peak results probably from disturbances during vibration. The distribution for (P) is slightly broader than that one for random packing of monosized spheres; Exp (A) from [17].

formed with monosized spheres,  $d = 2.3$  mm. The mean values are fairly close; the polydisperse sphere system results in a slightly broader distribution which agrees with the results from Matsushima and Blumenfeld [49].

In order to investigate the distributions in the bulk in more detail, subvolumes were used with cross-sections in the  $y$ - $z$  plane of  $15 \times 15$  mm and an inner zone in the  $x$ -direction of 14 mm. Table 5 shows that four of these subvolumes are located in the container corner regions with wall distances to the side walls of 5 mm; the fifth submodule was placed in the container center. The table contains for each subvolume the number of spheres,  $N_{\text{sph}}$ , and below the corresponding fractions of the  $d$ -groups. To the right, the mean  $\gamma_{\text{Vor}}$  is given and below the values for the  $d$ -groups. Considering that during vibration the upper right corner is at the highest elevation, there are the following trends: the large sphere fraction is smallest at the top and the largest at the lowest corner; the opposite trend exists for the small spheres.  $N_{\text{sph}}$  differs also between top and bottom corner. In all cases,  $\gamma_{\text{Vor}}$  increases with  $d$ . Because  $N_{\text{sph}}$  is smallest in the bottom subvolume,  $\gamma_{\text{Vor}}$  is also quite small for the large  $d$ -group. The largest  $\gamma_{\text{Vor}}$  values in the top corner are explained by the fact that vibration is most efficient in this zone during the increased vibration intensity in the last filling steps.

#### 4. Conclusions

We reported the first detailed experimental investigations of sphere packing structures in slender prismatic containers ( $X \ll Y = Z$ ), filled and vibrated with both monosized spheres (diameter  $d = 2.4$  mm;  $\approx 12\,300$  particles), Exp. (M), and polydisperse spheres ( $0.9 \text{ mm} < d < 1.25$  mm;  $\approx 105\,000$  particles), Exp. (P). The morphology and topology of the sphere packings were determined by three-dimensional X-ray CT, including characteristic quantities such as void fraction distributions, sphere center coordinates, coordination numbers, contact angle distributions and Voronoi packing fractions.

For (M),  $\gamma_t \approx 0.68$  was obtained which is close to the value for dense hexagonal packing for the used geometry. The hexagonal structure at the large vertical walls served as a template for crystallization in between. This kind of hexagonal dense packing dominated the largest part of the packing volume, confirmed by all quantities mentioned above. The re-

sults from (M) also point out that crystallization processes are significantly different compared to cylindrical containers.

Specific for the obtained structure is that the sphere densities in contact with the other container walls, the side walls, is much smaller than for a hexagonal array because, ideally, every second sphere is in a position with a defined distance to the wall. This results in void fraction distributions where the first wall minimum has a larger void fraction value than the second minimum. This behavior is also observed for the bottom walls (for the container orientation during vibration, there were two bottom walls) which means that many spheres are arranged in positions which do not occur with gravitational filling.

The obtained structures are not specific for the revolved arrangement of the container but were also observed for the prismatic container with a horizontal position of the bottom plate and applying 1d vertical vibration with a free particle bed surface.

Additional packing experiments with slender containers were performed, primarily with monosized spheres with different diameters in order to understand better the large  $\gamma_t$  obtained in (M). For other parameter values, large  $\gamma_t$  values are obtained as well. A simple relation is proposed in order to understand the occurrence of high  $\gamma_t$  values, valid for slender prismatic containers.

Although the diameter spread of (P) is quite small, very different results are obtained:  $\gamma_t \approx 0.62$ , regular structures are restricted to wall zones of  $\approx 4d$  thickness, and a non-ordered packing exists in a largest part of the volume. Similar results were obtained in several older publications with monosized spheres. However, two effects could have contributed to the previous results: i) the  $d$  spread was so large that these systems should have been considered as polydisperse systems, and ii) the densification of the particle bed was small. The use of the same 1d vertical vibration method for both the present experiments and the investigations in cylindrical containers with monosized spheres [17], including another polydisperse sphere system and binary spheres (content of a future publication) show that the much less developed structure in (P) is primarily caused by the use of non-monosized spheres. As compared to the monosized samples, it is evident that polydispersity results in less ordered wall layers which inhibit the ordering process within the granular media.

Table 5. Exp (P): Sphere numbers,  $N_{\text{sph}}$ , and Voronoi packing fractions  $\gamma_{\text{Vor}}$  for different subvolumes: see legend at top of table; 1<sup>st</sup> row:  $N_{\text{sph}}$  and mean  $\gamma_{\text{Vor}}$  of subvolume; below:  $N_{\text{sph}}$  fractions and  $\gamma_{\text{Vor}}$  for  $d$ -groups.

2796	0.647		$N_{\text{sph}}$	$\gamma_{\text{Vor}}$ all $d$		2815	0.648
0.324	0.634		fr 1.04	$\gamma_{\text{Vor}}$ 1.04		0.357	0.636
0.325	0.646		fr 1.11	$\gamma_{\text{Vor}}$ 1.11		0.334	0.649
0.351	0.659		fr 1.18	$\gamma_{\text{Vor}}$ 1.18		0.308	0.661
			2782	0.635			
			0.342	0.624			
			0.343	0.634			
			0.315	0.647			
2613	0.626					2734	0.643
0.262	0.612		0.289	0.630			
0.318	0.624		0.339	0.643			
0.419	0.636		0.372	0.654			

In technical applications with fluid flow through the packing, the use of polydisperse systems with a larger  $\lambda$  compared to (P) could be of interest in order to minimize the build-up of regular wall structures which give rise to non-uniform velocity distribution, unfavorable for several heat and mass transfer processes. In fusion reactor blankets [3, 37], however, heat, generated inside the particles, is transported primarily by conduction to the container walls. Containers are composed of slender prismatic units and large packing fractions are of prime design importance.

Further DEM simulations and experiments are recommended in order to identify: a) the maximum diameter spread which is tolerable for the generation of hexagonal dense packings, b) the effects of increasing  $X/d$  to also observe the crystallization dynamics originating from other walls, c) the optimization of vibration methods to achieve desirable topological structures.

## References

- [1] H. Jaeger, S. Nagel, R. Behringer: *Rev. Mod. Phys.* 69 (1996) 1259–273. DOI:10.1103/RevModPhys.69.1259
- [2] N. Kumar, O. Imole, V. Magnanimo, S. Luding: *Particuology* 12 (2014) 64–79. DOI:10.1016/j.partic.2013.07.011
- [3] Y. Gan, F. Hernandez, D. Hanaor, R. Annabattula, M. Kamlah, P. Pereslavtsev: arXiv:1406.4199v1 [cond-mat.soft] (2014). DOI:10.13182/fst13-727
- [4] S. Khirevich, A. Hölzel, A. Seider-Morgenstern, U. Tallarek: *J. Chromatogr. A* 1262 (2012) 77–91. PMID:23000179; DOI:10.1016/j.chroma.2012.08.086
- [5] O. Pouliquen, M. Nicolas, P. Weidman: *Phys. Rev. Lett.* 79 (1997) 3640–3643. DOI:10.1103/physrevlett.79.3640
- [6] T. Aste, M. Saadatfar, A. Sakellariou, T. Senden: *Physica A* 339 (2004) 16. DOI:10.1016/j.physa.2004.03.034
- [7] R.K. McGearry: *J. Am. Ceram. Soc.* 44 (1961) 513–522. DOI:10.1111/j.1151-2916.1961.tb13716.x
- [8] K. Dong, C. Wang, A. Yu: *Chem. Eng. Sci.* 126 (2015) 500–516. DOI:10.1016/j.ces.2014.12.059
- [9] M. Moscardini, Y. Gan, R. Annabattula, M. Kamlah: *Fusion Eng. Des.* 121 (2017) 22–31. DOI:10.1016/j.fusengdes.2017.05.110
- [10] R. Benenati, C. Brosilow: *AICHE J.* 8 (1962) 359–361. DOI:10.1002/aic.690080319
- [11] K. Ridgway, K. Tarbuck: *J. Pharm. Pharmacol.* 18 (1966) 168S–175S. DOI:10.1111/j.2042-7158.1966.tb07980.x
- [12] G. Scott: *Nature* 188 (1960) 908–909. DOI:10.1038/188908a0
- [13] M. Suzuki, T. Shimura, K. Limura, M. Hirota: *Adv. Powder Technol.* 19 (2008) 183–195. DOI:10.1163/156855208X293817
- [14] B. Gong, Y. Feng, H. Liao, X. Wu, S. Wang, X. Wang, K. Feng: *Fusion Eng. Des.* 121 (2017) 256–264. DOI:10.1016/j.fusengdes.2018.05.033
- [15] T. Owe Berg, R. McDonald, R. Trainor: *Powder Technol.* 3 (1969/70) 183–188. DOI:10.1016/0032-5910(69)80076-8
- [16] L. Vanel, A. Rosato, R. Dave: *Phys. Rev. Lett.* 78 (1997) 1255–1258. DOI:10.1103/PhysRevLett.78.1255
- [17] J. Reimann, J. Vicente, E. Brun, C. Ferrero, Y. Gan, A. Rack: *Powder Technol.* 318 (2017) 471–483. DOI:10.1016/j.powtec.2017.05.033
- [18] X. An, C. Li: *Particuology* 11 (2013) 689–694. DOI:10.1016/j.partic.2012.06.019
- [19] C. Li, X. An, R. Yang, R. Zou, A. Yu: *Powder Technol.* 208 (2011) 617–622. DOI:10.1016/j.powtec.2010.12.029
- [20] W. Dai, J. Reimann, D. Hanaor, C. Ferrero, Y. Gan; accepted for publication in *Granular Matter*.
- [21] R.I. Al-Raoush, C.S. Willson: *J. Hydrol.* 300 (2005) 44–64. DOI:10.1016/j.jhydrol.2004.05.005
- [22] J. Reimann, R. Pieritz, M. di Michiel, C. Ferrero: *Fusion Eng. Des.* 75–79 (2005) 1049–1053. DOI:10.1016/j.fusengdes.2005.06.223
- [23] J. Reimann, R. Pieritz, R. Rolli: *Fusion Eng. Des.* 81 (2006) 653–658. DOI:10.1016/j.fusengdes.2005.06.375
- [24] T. Aste, M. Saadatfar, T. Senden: *PhysRevE*.71, 061302 (2005). PMID:16089730; DOI:10.1103/PhysRevE.71.061302
- [25] K. Lochmann, L. Oger, D. Stoyan: *Solid State Sciences* 8 (2006) 1397–1413. DOI:10.1016/j.solidstatesciences.2006.07.011
- [26] Y. Jin, H. Maske: *Physica A* 389 (2010) 5362–5379. DOI:10.1016/j.physa.2010.08.010
- [27] G. Delaney, T. Di Matteo, T. Aste: *Soft Matter* 6 (2010) 2992–3006. DOI:10.1039/b927490a
- [28] F. Scaffidi-Argentina, G. Piazza, A. Goraieb, E. Boller: *Fusion Eng. Des.* 58–59 (2001) 707–712. DOI:10.1016/S0920-3796(01)00539-7
- [29] R. Al-Raoush, M. Alsaleh: *Powder Technol.* 176 (2007) 47–55. DOI:10.1016/j.powtec.2007.02.007
- [30] S. Torquato, Y. Jiao: *Nature* 460 (2009) 876–879. PMID:19675649; DOI:10.1038/nature08239
- [31] X. An, R. Yang, K. Dong, A. Yu: *Comput. Phys. Commun.* 182 (2011) 1989–1994. DOI:10.1016/j.cpc.2011.02.006
- [32] M. Saadatfar, H. Takeuchi, V. Robins, N. Francois, Y. Hiraoka: *Nat. Commun.* 8, (2017) 15082. PMID:28497794; DOI:10.1038/ncomms15082
- [33] K. Dong, C. Wang, A. Yu: *Chem. Eng. Sci.* 126 (2015) 500–516. DOI:10.1016/j.cpc.2011.02.006
- [34] Y. Wu, X. An, A. Yu: *Powder Technol.* 314 (2017) 89–101. DOI:10.1179/1432891714Z.00000000825
- [35] R. Farr: *Powder Technol.* 245 (2013) 28–34. DOI:10.1016/j.powtec.2013.04.009
- [36] R. Annabattula, Y. Gan, M. Kamlah: *Fusion Eng. Des.* 87 (2012) 853–858. DOI:10.1016/j.fusengdes.2012.02.033
- [37] F. Hernandez, P. Pereslavtsev, Q. Kang, P. Norajitra, B. Kiss, G. Nadasi, O. Blitz: *Fusion Eng. Design* 124 (2017) 882–886. DOI:10.1016/j.fusengdes.2017.02.008
- [38] A. Abou-Sena, H. Neuberger, T. Ihli: *Fusion Eng. Des.* 84 (2009) 355–358. DOI:10.1016/j.fusengdes.2008.11.064
- [39] J. Reimann, A. Abou-Sena, R. Nippen, C. Ferrero: *KIT SR* 7631 (2012).
- [40] J. Reimann, A. Abou-Sena, R. Nippen, P. Tafforeau: *Fusion Eng. Des.* 88 (2013) 234–237. DOI:10.1016/j.fusengdes.2013.05.100
- [41] J. Reimann, L. Boccaccini, M. Enoeda, A. Ying: *Fusion Eng. Des.* 61–62 (2002) 319–331. DOI:10.1016/S0920-3796(02)00214-4
- [42] R. Desu, A. Moorthy, R. Annabattula: *Fusion Eng. Des.* 127 (2018) 259–266. DOI:10.1016/j.fusengdes.2018.01.005
- [43] J. Reimann, E. Brun, C. Ferrero, J. Vicente: *Fusion Eng. Des.* 98–99 (2015) 1855–1858. DOI:10.1016/j.fusengdes.2015.05.026
- [44] J. Vicente, F. Topin, J.-V. Daurelle: *Mater. Trans.* 47 (2006) 2195–2202. DOI:10.2320/matertrans.47.2195
- [45] J. Mollicone, F. Ansart, P. Lenormand, B. Duployer, C. Tenailleu, J. Vicente: *J. Eur. Ceram. Soc.* 34 (2014) 3479–3487. DOI:10.1016/j.jeurceramsoc.2014.05.030
- [46] E. Brun, C. Ferrero, J. Vicente: *Fundamenta Informaticae* 155 (2017) 363–372. DOI:10.3233/FI-2017-1590
- [47] R. Zou, A. Yu: *Chem. Eng. Sci.* 50 (1995) 1504–1507. DOI:10.1016/0009-2509(94)00483-8
- [48] J. Duran, J. Rajchenbach, E. Clément: *Phys. Rev. Lett.* 70 (1993) 2431–2434. PMID:10053560; DOI:10.1103/PhysRevLett.70.2431
- [49] T. Matsushima, R. Blumenfeld: *Phys. Rev. Lett.* 112 (2014) 098003. PMID:24655281; DOI:10.1103/PhysRevE.95.032905

(Received October 30, 2018; accepted April 2, 2019)

## Correspondence address

Dr. Joerg Reimann  
 Institut für Kern und Energietechnik  
 Karlsruher Institut für Technologie, KIT  
 Postfach 3640  
 76021 Karlsruhe  
 Germany  
 Tel.: +49721811810  
 E-mail: joerg.reimann@partner.kit.edu; reimann-langhans@web.de

## Bibliography

DOI 10.3139/146.111814  
*Int. J. Mater. Res. (formerly Z. Metallkd.)*  
 110 (2019) E; page 1–13  
 © Carl Hanser Verlag GmbH & Co. KG  
 ISSN 1862-5282